Phase Control of Multivalent Vanadium Oxides VO$_x$ by Ion-Beam Sputter-Deposition

Martin Becker,* Jill Kessler, Florian Kuhl, Sebastian L. Benz, Limei Chen, Angelika Polity, Peter J. Klar, and Sangam Chatterjee

Vanadium–oxygen materials are of interest for various applications and fields of solid-state physics owing to the unequaled plethora of different phases. The wealth of phases and complexity of its phase diagram infer a strong sensitivity on the growth parameters for each phase. Thus, the reproducible growth of vanadium-oxide thin-films of defined phases by nonequilibrium techniques is challenging. Here, it is shown that ion-beam sputter-deposition (IBSD) is a powerful tool to reproducibly deposit defined polycrystalline vanadium oxide films by precisely controlling oxygen flux and substrate temperature in the growth process. Hence, it is demonstrated that IBSD has the potential to reliably produce binary phases (including unstable phases) from the vanadium–oxygen phase space. X-ray diffraction (XRD) and Raman spectroscopy are used to establish a map of the different crystalline phases dependent on the growth parameters. In particular, it is proved that thin-film V$_3$O$_7$ can be realized by IBSD and its Raman fingerprint is unambiguously identified.

1. Introduction

The metal–oxygen bonding in transition-metal oxides (TMOs) can vary between the extremes of a metallic and a completely ionic bonding. Furthermore, the transition metal ions can adopt their valence in a wide range according to their bonding environment. Consequently, TMOs exhibit an unusual range of electronic, magnetic, and optical properties. Some representatives offer an outstanding richness of different condensed matter phases, which are adjustable by choosing the right stoichiometry. Furthermore, structural phase transitions may occur at fixed stoichiometry as a function of temperature, pressure, excitation,

M. Becker, J. Kessler, F. Kuhl, S. L. Benz, L. Chen, A. Polity, P. J. Klar, S. Chatterjee
Institute of Experimental Physics I and Center for Materials Sciences (Zfm/LaMa)
Justus Liebig University Giessen
Heinrich-Buff-Ring 16, 35392 Giessen, Germany
E-mail: martin.becker@exp1.physik.uni-giessen.de

or composition. For instance, vanadium oxides comprise one such prototypical system. Its phases have triggered research in manifold applications such as batteries,[1–10] electrochromic devices,[11–16] and thermochromic smart windows.[17–20] The different possible oxidation states of vanadium allow for the formation of several binary phases with complex properties. Combinations of the four oxidation states (V^{2+}, V^{3+}, V^{4+}, or V^{5+}) belong to homologous series, the Magnéli phases V$_m$O$_{2m-1}$ ($m > 1$), and the Wadsley phases V$_m$O$_{2m+1}$, respectively. The "extreme" representatives of the Magnéli phases are V$_2$O$_3$ and VO$_2$ with a single oxidation state of V^{3+} and V^{4+}, respectively. Both VO$_2$ and V$_2$O$_3$ show a metal-to-insulator transition (MIT) with an abrupt change in optical and electrical properties.[21,22] The Wadsley phases can be considered as vanadium oxides arising from mixing VO$_2$ with the Magnéli phases. This family including V$_6$O$_{13}$, V$_3$O$_7$, and V$_2$O$_5$, exhibit average oxidation states in the range between V^{4+} and V^{5+}.

Thin films of the various vanadium oxides have been deposited by various techniques such as evaporative methods,[23,24] sputtering processes,[25–27] chemical vapor deposition,[28] atomic layer deposition,[29,30] pulsed laser deposition (PLD),[31,32] and hydrothermal synthesis.[33] In all cases, the formation of a specific phase can be selected in the growth process by adjusting the growth parameters. However, for most deposition methods not all known crystalline VO$_x$ phases can be realized within the boundaries of the available growth parameter space.

In case of ion-beam sputter deposition (IBSD), tuning parameters like oxygen flux, radio frequency (RF) power, or substrate temperature during the growth process allows one to selectively deposit thin films of defined V:O ratio as a pure phase or phase mixtures. Synthesis by sputtering ensures especially precise control over the stoichiometry of growing films and even enables the growth of metastable phases under nonequilibrium growth conditions.[34] However, several issues remain unclear despite the vast research efforts. Open questions are, for example, which deposition technique yields the best-quality thin films overall or is the best quality realized by a specific method rather phase specific or even application-dependent. The quality issue is particularly challenging as the morphology of the synthesized VO$_x$ also affects its properties and hence, the desired performance or application. For example, nanostructured

V_2O_5 is characterized by a large electrochemical surface area and good interconnectivity for electronic conductivity compared to the bulk material.[15] Thus, the electrochromic performances will depend on several parameters, including the coating processes which determine film morphology and thickness. Similarly, the MIT for both phases V_2O_3 and VO_2 is closely linked to the size and shape of the crystallite grains comprising the sample.[35,36]

Here, we demonstrate the immense capabilities of IBSD for controlled growth of virtually any desired phase of the multivalent vanadium oxide system. This unique versatility goes beyond any achieved by prior employed sputter techniques. It is enabled by the accurate control of the composition of the gas mixture of Ar and O_2 inside the ion source and thus in the growth process. This high degree of control of the reactive species in the growth process is one of the numerous advantages of IBSD. Others are its great flexibility in the choice of target material and sputter geometry. Furthermore, the gas discharge is contained inside the ion source and not in contact with the substrate and the deposited film. Thus, the plasma cannot infer materials damage. More information on the fundamentals of IBSD and its application in material processing can be found elsewhere.[37–39] Making use of these advantages, we grow thin films of vanadium oxides across an unprecedented compositional range using the same deposition technique and apparatus.

2. Results and Discussion

All crystalline phases of the VO_x thin films obtained by IBSD are mapped in **Figure 1** as a function of oxygen flux f_{O_2} and heater temperature during growth. The symbols denote individual samples. The dashed lines are guides to the eye for the boundaries between the growth regimes of different vanadium oxide phases.
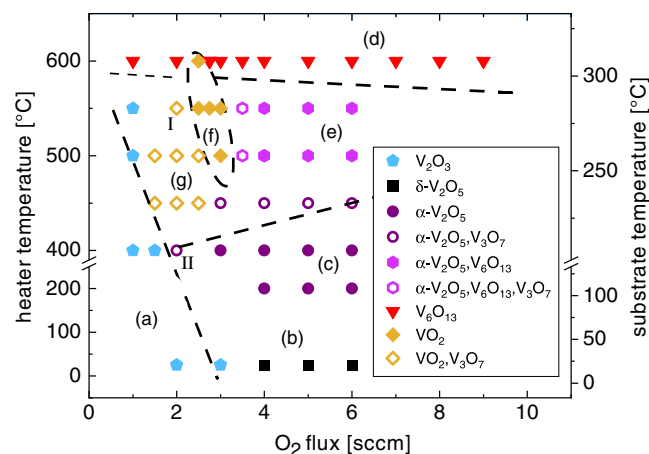

Figure 1. Map of the thin film phases as a function of oxygen flux and substrate temperature based on the X-ray diffraction (XRD) analysis and Raman spectroscopy. Clearly, different growth regions are addressed: a) V_2O_3 (pentagons), b) δ-V_2O_5 (squares), c) α-V_2O_5 (circles), d) V_6O_{13} (triangles), e) α-V_2O_5/V_6O_{13} (hexagons), f) VO_2 (diamonds), and g) samples potentially V_3O_7 (open symbols, the shape indicates possible admixtures of the adjacent phases VO_2 or V_2O_5). The Roman numerals designate two samples that will be used as examples in the following discussion.

We identify: a) V_2O_3 (pentagons), b) δ-V_2O_5 (squares), c) α-V_2O_5 (circles), d) V_6O_{13} (triangles), e) α-V_2O_5/V_6O_{13} (hexagons), f) VO_2 (diamonds), and g) V_3O_7 (open symbols, the shape indicates possible admixtures of the adjacent phases VO_2 or V_2O_5). The map is derived based on the results of XRD analysis and Raman spectroscopy. Note the two different ordinates indicating that nominal heater temperature and substrate surface temperature differ. In the following, we will discuss our results in terms of the (nominal) heater temperature, since this temperature is the one to be controlled and monitored in operando throughout the entire growth study (cf. Figure S1, Supporting Information for the calibration procedure).

Exemplary XRD patterns for seven different thin films are given in **Figure 2**. The broad reflection around 20°, seen in all diffractograms, is due to amorphous material. However, thin films grown at low heater temperatures and with oxygen fluxes below 3 sccm additionally exhibit the rhombohedral corundum structure of bulk V_2O_3, see Figure 2a. The diffractogram shows two distinct maxima at $2\theta = 38.8°$ and $2\theta = 64.87°$, which correspond to reflections from the planes (006) and (300), respectively.[40] Higher order reflections are not observed in the 2θ range shown. Both the reflections present in the thin film are at higher Bragg's angle as compared to those of the bulk material and, thus, there exists slight compressive strain along the growth direction. This out-of-plane compressive strain will produce an in-plane tensile strain. At higher heater temperatures, V_2O_3 changes to other phases or a phase mixture.

Increasing the oxygen fluxes above 3 sccm yet keeping low heater temperatures yields, at first sight, amorphous material, cf. Figure 2b. As shown in the following, the Raman spectra of this sample correspond to δ-V_2O_5. Figure 2c shows the XRD data for a polycrystalline α-V_2O_5 film that has been deposited at 200 °C with an oxygen flux of 6 sccm. Owing to the amorphous quartz substrate, a multitude of different out-of-plane orientations of the α-V_2O_5 polymorph is present in the corresponding diffractogram. The XRD data suggest that all films deposited at heater temperature above 600 °C are composed of V_6O_{13} regardless of the set oxygen fluxes. Exemplarily, XRD data for a thin film deposited with a reactive gas flow of 6 sccm are shown in Figure 2d. In total, we observe seven X-ray reflections at 2θ values of 17.82°, 27.01°, 36.22°, 45.66°, 55.46°, 64.70°, and 76.65°, respectively. All belong to the {001} family of planes. Keeping the oxygen flux above 3 sccm, in a rather broad range of heater temperatures between 400 °C and 600 °C neither V_6O_{13} nor α-V_2O_5 are obtained phase-pure, cf. Figure 2e. Interestingly, the V_6O_{13} phase still exhibits a preferential orientation along (001), independent of the α-V_2O_5 fraction included in the thin film. The α-V_2O_5 phase for these growth conditions, besides small traces of (110)-oriented crystallites exhibits mainly the low-index reflection (010) and its higher order reflection (020). Here, clearly, the presence of the additional V_6O_{13} phase triggers growth along low-index orientations with the relative intensity ratio of (010) and (110) being reversed in comparison with the unperturbed α-V_2O_5 growth. However, (010) being the most robust crystal orientation of α-V_2O_5 upon phase transformation to V_6O_{13} comes by no surprise, as (010) is the natural cleavage plane and possesses the lowest relaxed surface energy in the α-V_2O_5 structure.[41] Intriguingly, oxygen fluxes as low as 2.5–3 sccm access a small growth window for crystalline
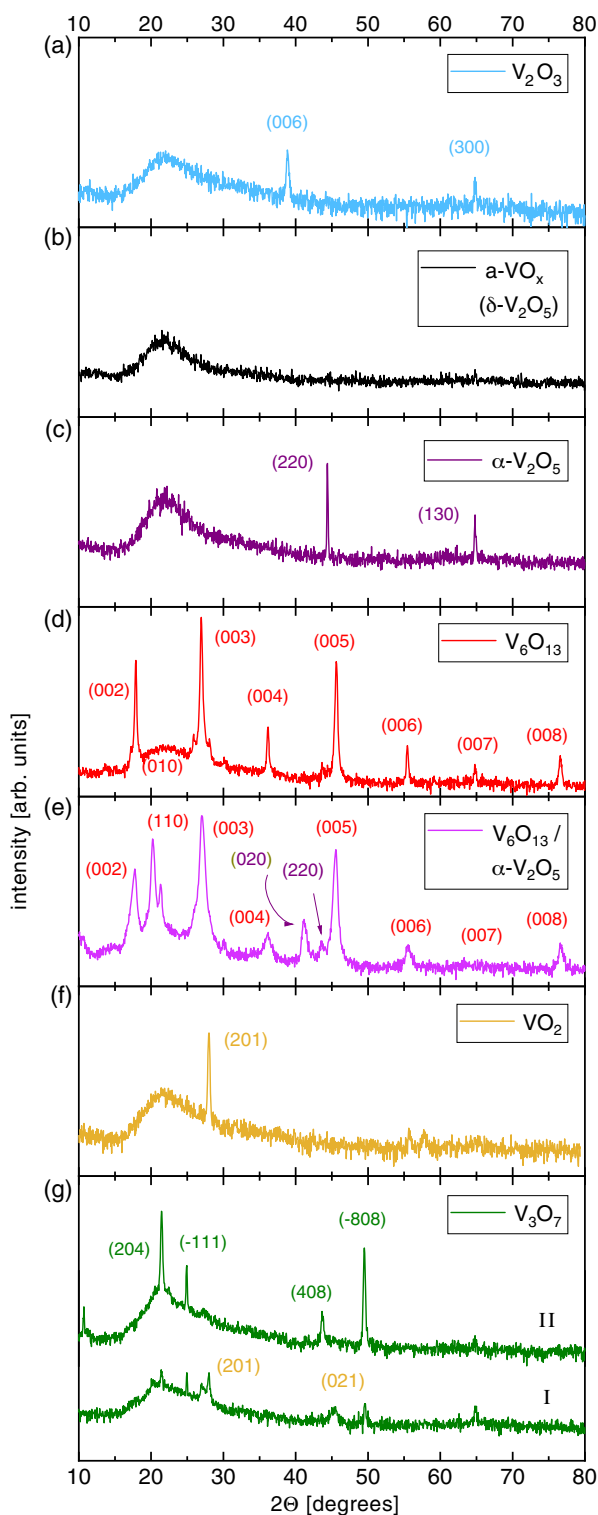
ADVANCED
SCIENCE NEWS
www.advancedsciencenews.com

physica
pss status solidi a

www.pss-a.com

Figure 2. XRD patterns of thin-film samples representative for the different growth regimes: a) V_2O_3, b) "amorphous" VO_x, c) α-V_2O_5, d) V_6O_{13}, e) α-V_2O_5/V_6O_{13}, f) VO_2, and g) top II): almost pure V_3O_7, bottom I): V_3O_7 with VO_2 secondary phase.

vanadium dioxide (VO_2) for heater temperatures above 500 °C. These films exhibit a preferential (011) orientation, cf. the

diffractogram of a thin film deposited at 550 °C heater temperature and 2.75 sccm oxygen flux in Figure 2f. Observing a reflection in this angular range is common for layers deposited on glass substrates, although it is often assigned to as (201) orientation of monoclinic VO_2.[42] However, (011) is the more convincing interpretation, as our layers are grown above the transition temperature and, thus, as VO_2 in its high-temperature rutile structure. Here, theoretical investigations on the low-index crystal surfaces and their stability suggest (110) to be the by far most stable surface dominating the equilibrium morphology.[43] As the rutile (110) surface corresponds to the monoclinic (011) surface, we expect this surface to dominate in our randomly oriented VO_2 crystallites.

Note that some diffractograms show additional reflections to those discussed in context with the distinct phases V_2O_3, α-V_2O_5, V_6O_{13}, and VO_2, or the α-V_2O_5/V_6O_{13} mixture. There exists another growth window between those of V_2O_3, VO_2, and α-V_2O_5, cf. open symbols in Figure 1. We assign this window to V_3O_7. The boundaries to the adjacent phases in the parameter space are rather broad. Thus, some of the samples belonging to this window exhibit an adjacent phase (indicated by the symbol shape) as a secondary phase. All assignments of the crystalline phases by XRD are supported by X-ray photoelectron spectroscopy (XPS) results, cf. depth profiles of exemplary samples in Figure S2, Supporting Information. In particular, the stoichiometry of the thin films of the phase-pure crystalline VO_x samples is confirmed by the XPS results, even when the samples exhibit an amorphous secondary phase. This strongly suggests that the secondary amorphous phase is of the same stoichiometry as the crystalline phase. This finding is somewhat anticipated as the V:O ratio can be accurately controlled in IBSD.

Figure 2g shows two diffractograms representative of samples of the V_3O_7 growth window. All sharp reflections can be assigned to those of polycrystalline V_3O_7 in case of the top trace.[44] In case of the lower trace, which corresponds to a sample grown with parameters closer to those of the VO_2 regime, additional sharp reflections occur which can be assigned to VO_2 as a secondary phase.

In this context, we would like to stress that the growth diagram presented in Figure 1 does not match expectations from the well-known Ellingham diagram, in which one might determine the stable vanadium oxide phase at a given combination of temperature and oxygen partial pressure.[45] However, as the Ellingham diagram is based on thermodynamic data for selected reactions in bulk material, it may not be used for determining the temperature ranges for metastable material in thin-film growth. Especially, as sputtering is known to facilitate thin film growth under nonequilibrium conditions and, thus, enables the formation of nonequilibrium phases not included in the Ellingham diagram.

Figure 3 depicts scanning electron microscopy (SEM) images of sample surfaces of thin films belonging to the different growth windows of the VO_x phases. First, we clearly stress the general influence of elevated temperatures on grain growth. Hence, a) V_2O_3, b) δ-V_2O_5, and c) α-V_2O_5, the phases grown at lower temperatures, exhibit smooth surfaces and consist of very small crystallites with a maximum size of a few nanometers, while the d) V_6O_{13}, e) α-V_2O_5/V_6O_{13}, and f) VO_2 thin films consist of grains of at least several 10 nm. The grain size of the VO_2 sample
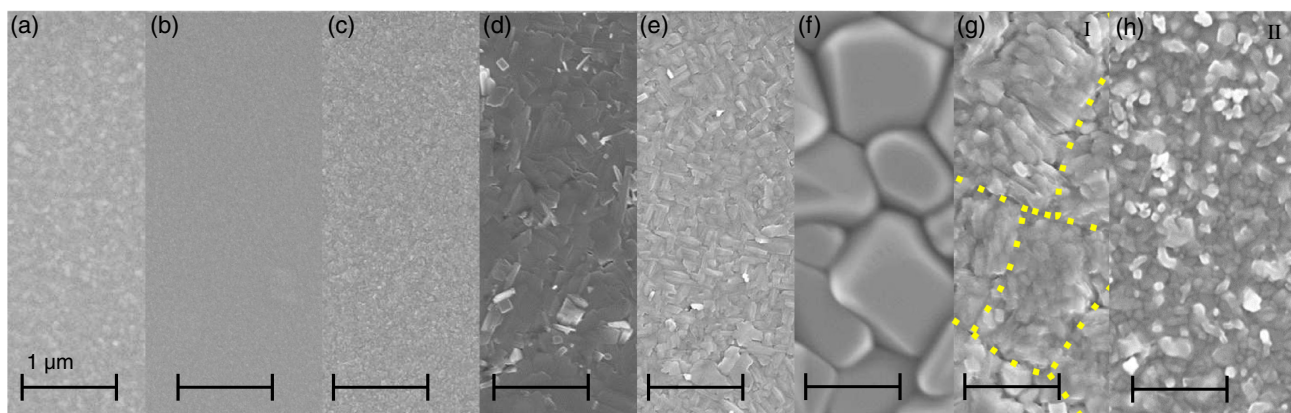
Figure 3. SEM images of thin-film samples representative for the different growth regimes: a) V_2O_3, b) δ-V_2O_5, c) α-V_2O_5, d) V_6O_{13}, e) α-V_2O_5/V_6O_{13}, f) VO_2, g) V_3O_7 with VO_2 secondary phase, and h) almost pure V_3O_7.

shown (550 °C, 2.75 sccm oxygen flux) is even around 1 μm. The surface of α-V_2O_5/V_6O_{13}, shown in Figure 3e, appears to consist of rectangular-shaped crystallites. These crystallites, however, are smaller than those typical for pure V_6O_{13} in Figure 3d, but are of a similar appearance. The decrease in size while keeping the shape somewhat corroborates the transition from V_6O_{13} to α-V_2O_5 with decreasing heater temperature revealed by the X-ray data. Figure 3g illustrates the surface of a sample grown at 550 °C and an oxygen flux of 2 sccm (sample I). The grains are obviously smaller than for the VO_2 sample grown at the same temperature but with a slightly higher oxygen flux, cf. Figure 3f.

Hence, the heater temperature is clearly not the only factor that influences the grain size: one rather has to carefully adjust the Ar:O_2 ratio as well. We tentatively expect V_3O_7 to be present at grain boundaries of dissembled VO_2 crystallites (yellow highlights in Figure 3g) since the sample at hand did also show V_3O_7-related reflections besides those of VO_2. Finally, Figure 3h shows an SEM image of almost pure V_3O_7 (sample II) with its multitude of small grains underlining the polycrystalline nature found in XRD.

Raman spectroscopy should provide additional means to identify clearly the phases occurring in the samples representative of the different growth regimes shown in Figure 1. In general, XRD and Raman results will yield the same assignments in terms of crystal structure. However, one method is more sensitive for identifying some polymorphs than the other and vice versa. Raman spectroscopy is particularly helpful in distinguishing different oxide phases in the case of large unit cells and low symmetry.[46,47] Depending on the Raman cross-sections of the phonons involved, it may be even more sensitive in identifying intermediate or secondary phases than XRD.

The normal modes and corresponding mode patterns of most vanadium oxide phases are well documented.[48] An exception is the Raman fingerprint of V_3O_7. Its Raman spectrum is controversially debated in the literature.[31,48–52] The difficulty arises because most VO_x phases can be considered as networks of VO_6 octahedral units sometimes with additional bipyramidal VO_5 units. The Raman spectra of the VO_x phases obviously are related to the vibrational modes of the corresponding polyhedral units. Thus similarities of the V_3O_7 Raman spectrum to those of, for instance, triclinic V_7O_{16},[31] and V_6O_{13},[50] are somewhat anticipated. For example, nominal V_3O_7 has been produced as nanofibers and nanoflowers.[51,52] The corresponding Raman spectra demonstrated features similar to α-V_2O_5 and additional bands at 848, 881, 932, and 1028 cm^{-1} for nanofibers or at 835, 871, 924, and 1021 cm^{-1} for nanoflowers. However, it has not been verified by XRD that the crystalline structure of the nanoscale samples is indeed V_3O_7.[51,52]

Figure 4 gives examples of typical Raman spectra of all phases under study. An overview of Raman-active phonons identified in this study in comparison with results of previous studies is given in Table S3, Supporting Information.

The Raman spectrum of V_2O_3 shows six distinct modes at 213, 234, 297, 335, 494, and 583 cm^{-1}, cf. Figure 4a. Some are rather broad and of low intensity. Below the phase transition temperature of 150–160 K, this vanadium oxide shows a monoclinic structure with space group C2c, whereas at higher sample temperatures V_2O_3 has a corundum structure (space group R$\bar{3}$c).[53–55] This change of crystal structure is accompanied by MIT. Thus, at room temperature, V_2O_3 is present in its corundum structure, where we expect seven Raman-active modes ($2A_{1g} + 5E_g$). Here, two vibrations, one with a mode pattern involving only movement of oxygen atoms and the other with a pattern arising from vanadium movement, yield the A_{1g} modes,[56] experimentally observed here at 234 and 494 cm^{-1}. Two E_g modes at 213 and 297 cm^{-1} are associated with the movement of vanadium atoms, whereas the remaining E_g modes are mainly associated with the motion of oxygen atoms. Two of these oxygen-related modes are found at 335 and 583 cm^{-1}, whereas the remaining E_g mode has not been observed experimentally.[57] Hence, no modes besides those related to V_2O_3 are present underlining phase purity of the material grown.

Figure 4b depicts the Raman spectrum of a sample identified as "amorphous" by XRD. The presented data clearly evidences that apparently a residual degree of crystallinity is found in the corresponding thin film. However, the Raman modes observed are rather broad and are somewhat shifted with respect to the modes of V_2O_5 samples deposited at slightly higher heater temperatures, cf. Figure 4c. This deviation may be explained when considering that V_2O_5 crystallizes in at least six
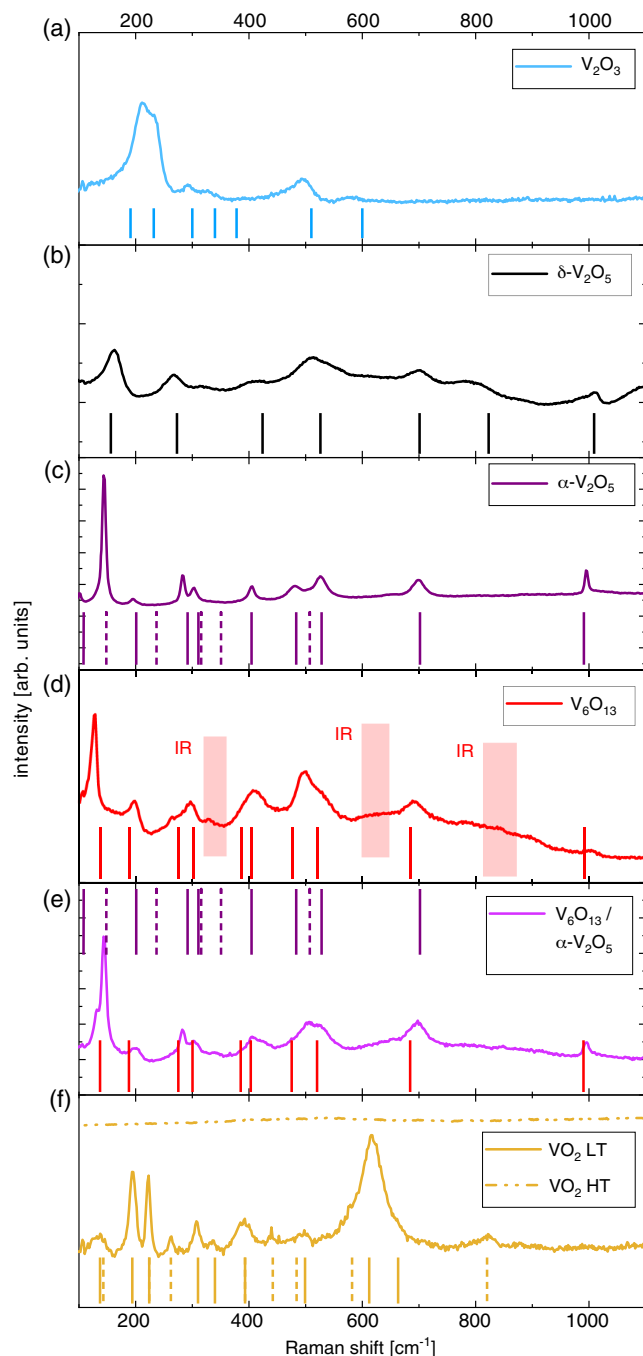
Figure 4. Raman spectra of representative layers of: a) V_2O_3, b) δ-V_2O_5, c) α-V_2O_5, d) V_6O_{13}, e) α-V_2O_5/V_6O_{13}, f) VO_2, respectively. The additional vertical lines depict references from literature given for V_2O_3,[57] V_6O_{13},[62] V_2O_5,[61] and VO_2.[64].

polymorphs, namely α-V_2O_5, β-V_2O_5, γ-V_2O_5, δ-V_2O_5, η-V_2O_5, and ε-V_2O_5. The presumably best-known representative is orthorhombic α-V_2O_5.[58] The α-V_2O_5 structure is associated with 21 Raman-active modes ($7A_{1g} + 3B_{1g} + 7B_{2g} + 4B_{3g}$). Experimentally, the lowest wavenumber mode is an A_{1g} mode at 102 cm^{-1}. The other six A_{1g} modes are located at 196, 304,

405, 478, 526, and 995 cm^{-1}. The 995 cm^{-1} mode also includes a B_{2g} line. Additional Raman-active modes are observed at 145, 282, and 698 cm^{-1}, which incorporate contributions of B_{1g}, B_{2g}, and B_{3g} modes. Exemplarily, the dominant mode observed at 145 cm^{-1} incorporates contributions of one B_{1g}, one B_{2g}, and one B_{3g} mode. A more detailed discussion of the underlying vibrations can be found elsewhere.[48,59,60] Thus, in contrast to samples grown at higher heater temperatures and clearly assigned to α-V_2O_5, cf. Figure 4c, we observe spectra of δ-V_2O_5 for samples grown at lower heater temperatures, cf. Figure 4b, in agreement with the results of Zibrov et al.[61]

Figure 4d shows the Raman spectrum measured for a V_6O_{13} sample, deduced following the XRD results. It shows clear alikeness with the spectrum of α-V_2O_5, cf. Figure 4c, although there exist changes in relative intensity and small Raman shifts. The reason is the similarity of structural polyhedral units. Experimentally, Raman scattering for the monoclinic high-temperature phase presented here ($18A_g + 9B_g$ Raman-active modes) has been reported for microcrystalline powder,[62] nanobelts,[63] a single crystal,[23] and thin films.[23,25] Especially the spectra of the latter strongly resemble that of α-V_2O_5 in agreement with our results. In addition to indicating the positions of the Raman-active modes in Figure 4d, we mark additional frequency ranges in the spectrum where the IR-active modes should be located. It should be noted, that these are not expected to be Raman active in ideal V_6O_{13} films. Nonetheless, some V_6O_{13} spectra do exhibit traces of those modes, which presumably are Raman-activated by a structural disorder. Thus, the degree of their absence is a measure of the crystal quality of the layers. Here, those modes are mostly suppressed. Thus, the quality of IBSD-grown V_6O_{13} is rather good.

Figure 4e illustrates the spectrum of a representative α-V_2O_5/V_6O_{13} mixed-phase sample. Comparing the results of phase-pure α-V_2O_5 and V_6O_{13}, cf. Figure 4c,d, we see that the spectrum effectively can be understood as a blend of both constituents: for example, the most dominant feature at about 140 cm^{-1} consists of the main contribution at 144.4 cm^{-1} and a shoulder at 130.9 cm^{-1}. Additionally, we identify another feature for the α-V_2O_5/V_6O_{13} mixed phase, which is the broad, asymmetric feature around 500 cm^{-1}. In this region, both α-V_2O_5 and V_6O_{13} exhibit two Raman-active modes as seen in Figure 4c,d. For α-V_2O_5 the 481 cm^{-1} mode shows a lower intensity compared to that of the mode at 527 cm^{-1}, whereas for V_6O_{13} the 497 cm^{-1} mode shows a higher intensity compared to that of the mode at 530 cm^{-1}. Thus, the relative intensity of these two contributions or the asymmetry of the resulting superposition may serve as a fingerprint to distinguish between both constituents or to estimate the α-V_2O_5:V_6O_{13} ratio provided the absolute Raman-scattering cross-section are known.

VO_2 undergoes a reversible phase transition from an insulating to a metallic state at a temperature of 68 °C. This structural phase transition is also reflected in the Raman spectra recorded below and above the transition temperature. We show Raman spectra of a VO_2 sample taken at room temperature (VO_2 LT, solid line) and at 90 °C (VO_2 HT, dash-dotted line) in Figure 4f. As expected, for the metallic state, we observe no significant features in the spectrum. At room temperature, however, we observe a set of well-resolved Raman bands, the most prominent occurring at around 194, 224, and 610 cm^{-1}. The

monoclinic VO_2 structure is associated with 18 Raman-active vibrations $(9A_g + 9B_g)$.[64–66] The modes at 136, 194, 221, 309, 338, 389, 618, and 662 cm^{-1} are assigned to A_g phonons, whereas the modes at 136, 221, 261, 389, 441, 578, and 821 cm^{-1} are attributed to B_g symmetry. Obviously, near 136, 221, and 389 cm^{-1} A_g and B_g lines overlap and have yet to be resolved experimentally. Following the assignment of Shibuya and Sawa,[64] A_g and B_g modes are given as solid and dashed lines in Figure 4f, respectively. All Raman-active modes, including the B_g mode predicted at 450 cm^{-1} are visible in the spectrum obtained for IBSD-grown VO_2. Therefore, we assume that the crystalline VO_2 film obtained is of high quality. It is worth noting that two monoclinic VO_2 phases exist, referred to as M1 and M2.[67] The Raman-active modes observed in Figure 4f are indicative of the M1 phase. Group theory predicts the same number of Raman-active modes for the M2 phase changing only their character.[68] Consequently, the Raman spectra of the M1 and M2 phases differ only in peak positions and intensities, not in the overall peak pattern. The main difference is the appearance of a Raman mode at 640 cm^{-1} for the M2 phase. However, this feature is not present in our data. Thus, we are quite confident with our assignment of the M1 phase.

Finally, we discuss the Raman spectrum of V_3O_7-based samples obtained in the corresponding growth regime presented in cf. Figure 1. **Figure 5** shows the Raman spectra of two such samples as black curves. The results analyzed in graphs (a) and (b) are those of the same two samples whose XRD traces are shown in Figure 2g. According to the XRD analysis, the V_3O_7 samples corresponding to the Raman spectra in graphs (a) and (b) are a V_3O_7 thin film with VO_2 as a secondary phase (sample I) and almost pure V_3O_7 thin film with some amorphous regions (sample II). As the boundaries of the growth window of V_3O_7 are somewhat blurred, it cannot be ruled out that the Raman spectra plotted in black contain contributions of the phases of the adjacent growth windows, i.e., VO_2 (as already visible in the XRD trace of one of the two samples) and α-V_2O_5 (not detected by XRD). We have to rule out such contributions. When comparing the two Raman spectra plotted in black, it becomes obvious that there are slight differences between the spectra. In particular, the spectrum shown in (a) of sample I, exhibits an additional prominent feature at about 600 cm^{-1}, which does not occur in the spectrum in (b) of sample II. We scaled the intensity of the LT VO_2 spectrum (shown in Figure 4f), plotted in yellow in Figure 5 to remove the VO_2 contribution from the black spectrum. Similarly, we proceeded with the spectrum of α-V_2O_5 (shown in Figure 4c), plotted in magenta in Figure 5. The spectra of both possible contributions are plotted on the same scale as the black spectrum. It can be seen that the α-V_2O_5 contribution to the spectrum is rather small or almost negligible in accordance with the XRD data. The green curve shows the V_3O_7 spectrum corrected for the contributions of the other phases. Similarly, we proceeded with the black Raman spectrum in graph (b) of sample II, which is a nominally single phase according to the XRD data. We find that the estimated contributions of VO_2 (yellow curve) and α-V_2O_5 (magenta curve) are indeed negligible confirming the XRD results. The main features in the two corrected Raman spectra (green) of V_3O_7 are very similar especially at high wavenumbers, the differences in the prominent double feature at about 200 cm^{-1} are a bit more pronounced. A likely
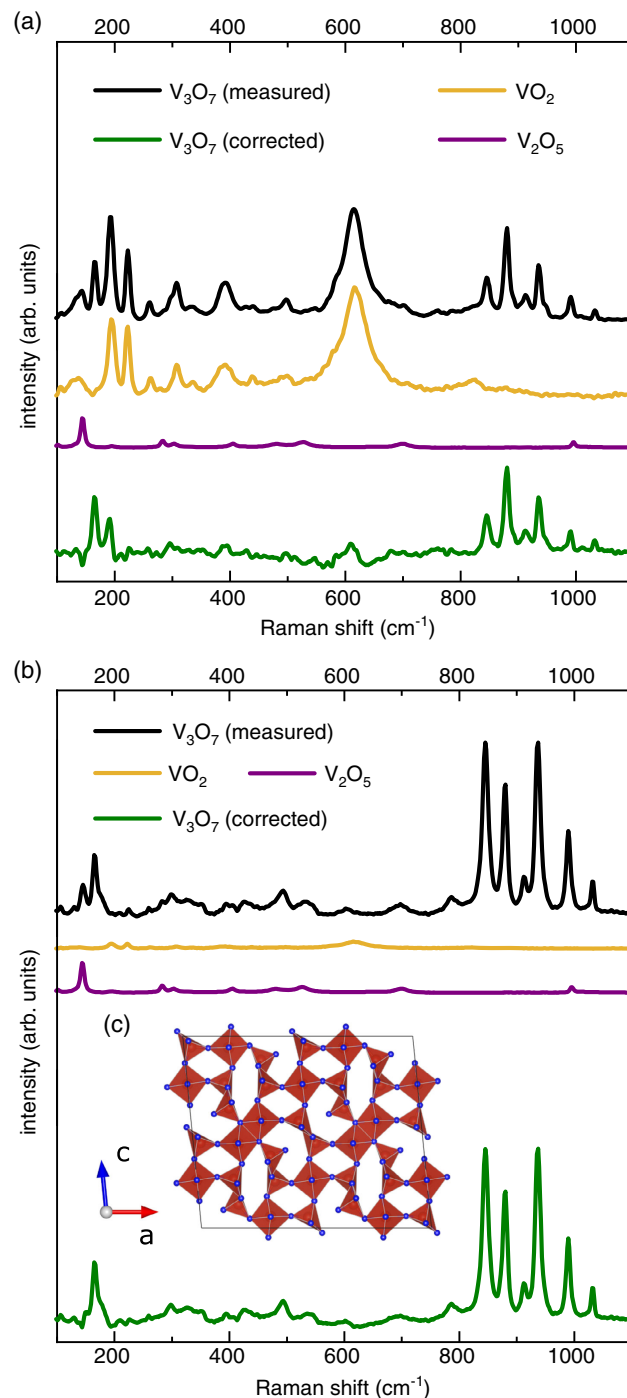

Figure 5. a,b) Raman spectra of two samples with V_3O_7-related features. Raman spectra obtained for VO_2 and α-V_2O_5 have been subtracted from the as-measured spectra to extract Raman spectra representative for phase-pure V_3O_7. The inset c) illustrates the unit cell of monoclinic V_3O_7 in polygon representation projected on (010).

reason is that the orientation of the V_3O_7 grains is somewhat different in the two samples according to the XRD traces which may lead to relative intensity variations of the observed Raman modes.

**ADVANCED
SCIENCE NEWS**

www.advancedsciencenews.com

pss
physica status solidi a

www.pss-a.com

It should be noted that other explanations for these modes can be found in the literature.[31,49,50] Features of an intermediate structure at 70, 155, 251, 695, 841, 880, 929, 981, and 1027 cm^{-1} have been observed for V_2O_5 xerogel samples.[49] Similar Raman spectra have been reported for pulsed laser deposited as well as magnetron sputtered films.[31,50] The structure of the sputter-grown films has been referred to as V_6O_{13},[50] while a V_7O_{16} triclinic cell has been stated for the PLD grown samples.[31] In both cases, however, the Raman spectrum was equivalent to the spectrum measured before [49] and especially not to the V_6O_{13} spectrum reported in the present work. Since sample degradation induced by increased laser irradiation power in Raman spectroscopy cannot be ruled out, nanostructures may decompose into an intermediate structure. Thus, very likely previous works did in fact observe V_3O_7. In our work, however, we already confirmed V_3O_7 in the XRD patterns, cf. Figure 2, which would then be one of the scarce presentations of directly grown V_3O_7 samples. Thus, we believe that the strongest Raman bands located at 165, 845, 881, 912, 937, 990, and 1031 cm^{-1} do indeed represent V_3O_7. These Raman frequencies are in good agreement with previous reports,[51,52] see also Table S3, Supporting Information.

According to the XRD analysis of Waltersson et al. on a single crystal,[44] crystalline V_3O_7 possesses a monoclinic unit cell, space group $C2c$ containing 12 units of V_3O_7, yielding a total of 120 atoms per unit cell corresponding to almost 360 vibrational modes. A group-theoretical analysis yields 90 Raman active modes ($44A_g + 46B_g$). The discrepancy between numbers of predicted and observed Raman modes can be better understood, when considering the unit cell of the V_3O_7 lattice in polygon representation projected on (010) in Figure 5c; or as an enlarged ball-and-stick representation in the Supporting Information. The unit cell is a network of VO_6 octahedra and VO_5 bipyramids. One can identify a chain of corner-sharing octahedral units and a chain containing pairs of edge-sharing octahedral units. Furthermore, one finds three types of VO_5 bipyramids within the unit cell, one type exhibiting a V=O double bond. An unperturbed VO_6 octahedra (O_h symmetry) exhibits three distinct Raman signals ($A_{1g} + E_g + F_{2g}$) and an unperturbed VO_5 bipyramid (D_{3h} symmetry) shows 6 distinct Raman features ($2A_1' + 3E' + E''$) in its spectrum. Neglecting symmetry reduction, but taking into account the five types of polygons occurring in the unit cell already yields 24 different Raman signals. The degenerate modes (e.g., twofold degenerate E or threefold degenerate F modes) can split further and additional modes (i.e., originally silent or IR active) may become Raman active due to the symmetry reduction at the sites of the polyhedra. This accounts for the 90 modes expected from the group-theoretical analysis based on the atomic positions in the unit cell. However, how many of these modes are at similar frequencies cannot be predicted, explaining the smaller number of distinct Raman peaks in the spectra. It may be anticipated that the strongest modes in the spectra involve vibrational patterns reflecting those of the strongest modes in the polyhedral units. It is worth noting that the charge state of the central V ions of the octahedral and bipyramidal polygons is 4+ and 5+, respectively. This implies that the high-frequency modes above 800 cm^{-1} are due to vibrations mainly involving the VO_5 bipyramidal units because of the stronger bonding due to the higher valence of their central V ions. In particular, the mode above 1000 cm^{-1} is most likely to have a mode pattern strongly involving the strong V=O double bond, similar to the findings for V_2O_5.[69]

3. Conclusion

We demonstrate that ion-beam sputter-deposition is a powerful tool to reliably deposit vanadium oxides of different stoichiometries. The whole range of Wadsley phases as well as the Magnéli phases V_2O_3 and VO_2 are obtained. In particular, we are able to grow polycrystalline V_3O_7 and determine its Raman spectrum. The transition regions between the growth windows of the various phases need to be evaluated carefully since mixtures of different phases are likely to occur in the rather blurred boundary regions. Nonetheless, this work paves the way for a reproducible sputter fabrication of a plethora of phase pure VO_x thin films of different valence (mixture). Such well-defined VO_x samples will not only help obtain a better understanding of the outstanding material properties of the vanadium oxide system but will also advance many applications involving vanadium oxide phases, especially in cases where large-scale deposition is not the main obstacle to overcome.

4. Experimental Section

Vanadium oxide thin films are deposited using IBSD. Here, an RF plasma was generated inside the ion source.[39] The pre-mixed gas composition of 2 sccm inert Ar and a variable amount of reactive O_2 were led into the discharge chamber, which was surrounded by an RF-induction coil operating at 2 MHz. The ion extraction was accomplished by grid-shaped electrodes in a three-grid configuration using the "accel-decel" technique. Ions of the plasma entering the extraction channel were accelerated onto the 4″ vanadium target, which was mounted under an ion incidence angle of 45° and in 20 cm distance to the outermost extraction grid. Typical ion currents were 30–35 mA. The vanadium sputtered off the metallic target and it reacted with the oxygen species of the ion beam forming a film of vanadium oxide on the substrate surface. The substrate-target distance was 15 cm and the polar emission angle was given as 5°. Here, fused silica was used as substrate material. The heater temperature was adjusted in the range of 25–600 °C depending on the desired phase. Typical growth rates varied between 1 and 4 nm min^{-1} (dependent on the argon–oxygen ratio and substrate temperature) when running the ion source with a power of 220 W. All layers discussed in this work exhibited a minimum thickness of 100 nm. A scheme of the IBSD setup and a more detailed description can be found elsewhere.[39,46]

X-ray diffraction (Siemens D 5000) in the θ–2θ geometry using Cu K_α radiation provides a structural and compositional analysis of all films. Raman spectra using 532 nm laser excitation and a spectral resolution of 1.5 cm^{-1} (Renishaw inVia Raman microscope system) provide complementary structural information. The morphology of the sample surfaces is studied by scanning electron microscope (SEM) using a Zeiss MERLIN SEM equipped with an InLens detector. The composition of the doped thin films is determined by XPS using an PHI VersaProbe II spectrometer, utilizing monochromatic Al K_α (1486.6 eV) radiation (for further information see Supporting Information).

Supporting Information

Supporting Information is available from the Wiley Online Library or from the author.

Acknowledgements

Conflict of Interest

The authors declare no conflict of interest.

Data Availability Statement

The data that support the findings of this study are available from the corresponding author upon reasonable request.

Keywords

[1] R. Yu, C. Zhang, Q. Meng, Z. Chen, H. Liu, Z. Guo, *ACS Appl. Mater. Interfaces* **2013**, *5*, 12394.

[2] I. D. Johnson, N. Stapleton, G. Nolis, D. Bauer, P. Parajuli, H. D. Yoo, L. Yin, B. J. Ingram, R. F. Klie, S. Lapidus, J. A. Darr, J. Cabana, *Nanoscale* **2021**, *13*, 10081.

[3] Y. Tang, X. Rui, Y. Zhang, T. M. Lim, Z. Dong, H. H. Hng, X. Chen, Q. Yan, Z. Chen, *J. Mater. Chem. A* **2013**, *1*, 82.

[4] X. Ren, Y. Zhai, L. Zhu, Y. He, A. Li, C. Guo, L. Xu, *ACS Appl. Mater. Interfaces* **2016**, *8*, 17205.

[5] S. Caes, J. C. Arrebola, N. Krins, P. Eloy, E. M. Gaigneaux, C. Henrist, R. Cloots, B. Vertruyen, *J. Mater. Chem. A* **2014**, *2*, 5809.

[6] I. Mjejri, N. Etteyeb, F. Sediri, *J. Alloys Compd.* **2014**, *611*, 372.

[7] S. Tepavcevic, H. Xiong, V. R. Stamenkovic, X. Zuo, M. Balasubramanian, V. B. Prakapenka, C. S. Johnson, T. Rajh, *ACS Nano* **2012**, *6*, 530.

[8] L. L. Zhang, G. Liang, A. Ignatov, M. C. Croft, X. Q. Xiong, I. M. Hung, Y. H. Huang, X. L. Hu, W. X. Zhang, Y. L. Peng, *J. Phys. Chem. C* **2011**, *115*, 13520.

[9] M. Simões, Y. Mettan, S. Pokrant, A. Weidenkaff, *J. Phys. Chem. C* **2014**, *118*, 14169.

[10] L. Yu, J. Xi, *ACS Appl. Mater. Interfaces* **2016**, *8*, 23425.

[11] Y. Iida, Y. Kaneko, Y. Kanno, *J. Mater. Process. Technol.* **2008**, *197*, 261.

[12] M. Kovendhan, D. P. Joseph, P. Manimuthu, A. Sendilkumar, S. N. Karthick, S. Sambasivam, K. Vijayarangamuthu, H. J. Kim, B. C. Choi, K. Asokan, C. Venkateswaran, R. Mohan, *Curr. Appl. Phys.* **2015**, *15*, 622.

[13] Y. Yang, D. Kim, P. Schmuki, *Electrochem. Commun.* **2011**, *13*, 1021.

[14] Y. Wei, J. Zhou, J. Zheng, C. Xu, *Electrochim. Acta* **2015**, *166*, 277.

[15] W. Kang, C. Yan, X. Wang, C. Y. Foo, A. W. M. Tan, K. J. Z. Chee, P. S. Lee, *J. Mater. Chem. C* **2014**, *2*, 4727.

[16] Z. Tong, H. Yang, L. Na, H. Qu, X. Zhang, J. Zhao, Y. Li, *J. Mater. Chem. C* **2015**, *3*, 3159.

[17] D. H. Qiu, Q. Y. Wen, Q. H. Yang, Z. Chen, *Mater. Sci. Semicond. Process* **2014**, *27*, 140.

[18] M. M. Seyfouri, R. Binions, *Sol. Energy Mater. Sol. Cells* **2017**, *159*, 52.

[19] W. Li, S. Ji, K. Qian, P. Jin, *J. Colloid Interface Sci.* **2015**, *456*, 166.

[20] H. Zhang, X. Xiao, X. Lu, G. Chai, Y. Sun, Y. Zhan, G. Xu, *J. Alloys Compd.* **2015**, *636*, 106.

[21] C. Wu, F. Feng, Y. Xie, *Chem. Soc. Rev.* **2013**, *42*, 5157.

[22] Z. Zhang, Y. Gao, Z. Chen, J. Du, *Langmuir* **2010**, *26*, 10738.

[23] A. Gorenstein, A. Khelfa, J. P. Guesdon, G. A. Nazri, O. M. Hussain, I. Ivanov, C. Julien, *Solid State Ionics* **1995**, *76*, 133.

[24] V. Théry, A. Boulle, A. Crunteanu, J. C. Orlianges, A. Beaumont, R. Mayet, A. Mennai, F. Cosset, A. Bessaudou, M. Fabert, *J. Appl. Phys.* **2017**, *121*, 055303.

[25] X. J. Wang, H. D. Li, Y. J. Fei, X. Wang, Y. Y. Xiong, Y. X. Nie, K. A. Feng, *Appl. Surf. Sci.* **2001**, *177*, 8.

[26] M. K. Dietrich, B. G. Kramm, M. Becker, B. K. Meyer, A. Polity, P. J. Klar, *J. Appl. Phys.* **2015**, *117*, 185301.

[27] F. Kuhl, M. Becker, S. L. Benz, J. Hauptmann, J. Kessler, S. Chatterjee, A. Polity, P. J. Klar, *ACS Applied Electronic Materials* **2022**.

[28] M. B. Sahana, S. A. Shivashankar, *J. Mater. Res.* **2004**, *19*, 2859.

[29] T. Singh, S. Wang, N. Aslam, H. Zhang, S. Hoffmann-Eifert, S. Mathur, *Chem. Vap. Deposit.* **2014**, *20*, 291.

[30] K. Manjunath, R. Singh, D. P. Panda, C. N. R. Rao, *Phys. Status Solidi RRL* **2021**, *15*, 2000565.

[31] J. Huotari, J. Lappalainen, J. Eriksson, R. Bjorklund, E. Heinonen, I. Miinalainen, J. Puustinen, A. L. Spetz, *J. Alloys Compd.* **2016**, *675*, 433.

[32] V. S. Vijay, R. Varghese, A. Sakunthala, S. Rajesh, B. Vidhya, *Vacuum* **2021**, *187*, 110097.

[33] M. Pradhan, A. Roy, A. K. Sinha, R. Sahoo, T. Deb, T. Pal, *Dalton Trans.* **2015**, *44*, 1889.

[34] M. Ohring, in *The Material Science of Thin Films*, Academic Press, San Diego **1992**.

[35] L. L. Fan, S. Chen, Z. L. Luo, Q. H. Liu, Y. F. Wu, L. Song, D. X. Ji, P. Wang, W. S. Chu, C. Gao, C. W. Zou, Z. Y. Wu, *Nano Lett.* **2014**, *14*, 4036.

[36] L. Kang, Y. Gao, H. Luo, Z. Chen, J. Du, Z. Zhang, *ACS Appl. Mater. Interfaces* **2011**, *3*, 135.

[37] M. Nastasi, J. W. Mayer, J. K. Hirvonen, in *Ion-Solid Interactions: Fundamentals and Applications*, 1st ed., Cambridge University Press, Cambridge, **1996**.

[38] C. Bundesmann, H. Neumann, *J. Appl. Phys.* **2018**, *124*, 231102.

[39] M. Becker, M. Gies, A. Polity, S. Chatterjee, P. J. Klar, *Rev. Sci. Instrum.* **2019**, *90*, 023901.

[40] W. R. Robinson, *Mater. Res. Bull.* **1974**, *9*, 1091.

[41] J. Goclon, R. Grybos, M. Witko, J. Hafner, *J. Phys.: Condens. Matter* **2009**, *21*, 095008.

[42] G. Fu, A. Polity, N. Volbers, B. K. Meyer, *Thin Solid Films* **2006**, *515*, 2519.

[43] T. A. Mellan, R. Grau-Crespo, *J. Chem. Phys.* **2012**, *137*, 154706.

[44] K. Waltersson, B. Forslund, K.-A. Wilhelmi, S. Andersson, J. Galy, *Acta Crystallogr.* **1974**, *B30*, 2644.

[45] I. Yamaguchi, T. Manabe, T. Tsuchiya, T. Nakajima, M. Sohma, T. Kumagai, *Jpn. J. Appl. Phys.* **2008**, *47*, 1022.

[46] M. Becker, A. Polity, P. J. Klar, B. K. Meyer, *Phys. Status Solidi RRL* **2015**, *9*, 326.

[47] B. Eifert, M. Becker, C. T. Reindl, M. Giar, L. Zheng, A. Polity, Y. He, C. Heiliger, P. J. Klar, *Phys. Rev. Mat.* **2017**, *1*, 014602.

[48] P. Shvets, O. Dikaya, K. Maksimova, A. Goikhman, *J. Raman Spectrosc.* **2019**, *50*, 1226.

[49] A. G. Souza Filho, O. P. Ferreira, E. J. G. Santos, J. Mendes Filho, O. L. Alves, *Nano Lett.* **2004**, *4*, 2099.

[50] C. Zhang, Q. Yang, C. Koughia, F. Ye, M. Sanayei, S.-J. Wen, S. Kasap, *Thin Solid Films* **2016**, *620*, 64.

[51] R. Berenguer, M. O. Guerrero-Perez, I. Guzman, J. Rodriguez-Mirasol, T. Cordero, *ACS Omega* **2017**, *2*, 7739.

[52] J. Ma, Q. Wu, Y. Chen, *Mater. Res. Bull.* **2009**, *44*, 1142.

[53] D. B. McWhan, J. P. Remeika, *Phys. Rev. B* **1970**, *2*, 3734.

[54] G. Andersson, *Acta Chem. Scand.* **1954**, *8*, 1599.

[55] X.-B. Chen, J.-H. Shin, H.-T. Kim, Y.-S. Lim, *J. Raman Spectrosc.* **2012**, *43*, 2025.

[56] E. R. Cowley, *Can. J. Phys.* **1969**, *47*, 1381.

[57] H. Yang, R. J. Sladek, *Phys. Rev. B* **1985**, *32*, 6634.

[58] R. Enjalbert, J. Galy, *Acta Crystallogr.* **1986**, *B42*, 1467.

[59] T. R. Gilson, O. F. Bizri, N. Cheetham, *J. Chem. Soc., Dalton Trans.* **1973**, *3*, 291.

[60] R. Baddour-Hadjean, M. B. Smirnov, V. Y. Kazimirov, K. S. Smirnov, J.-P. Pereira-Ramos, *J. Raman Spectrosc.* **2015**, *46*, 406.

[61] I. P. Zibrov, V. P. Filonenko, S. G. Lyapin, V. A. Sidorov, *High Pressure Res.* **2013**, *33*, 399.

[62] C. Julien, G. A. Nazri, O. Bergstrom, *Phys. Status Solidi B* **1997**, *201*, 319.

[63] H. Zeng, Y. Tang, W. Zou, C. Wang, H. Tao, Y. Wu, *ACS Appl. Nano Mater.* **2021**, *4*, 4654.

[64] K. Shibuya, A. Sawa, *J. Appl. Phys.* **2017**, *122*, 015307.

[65] F. U. Begara, A. Crunteanu, J.-P. Raskin, *Appl. Surf. Sci.* **2017**, *403*, 717.

[66] R. Srivastava, L. L. Chase, *Phys. Rev. Lett.* **1971**, *27*, 727.

[67] A. Oyiza Suleiman, S. Mansouri, N. Émond, B. Le Drogoff, J. Théophile Bégin, *Sci. Rep.* **2021**, *11*, 1620.

[68] C. Marini, E. Arcangeletti, D. Di Castro, L. Baldassare, A. Perucchi, *Phys. Rev. B* **2008**, *77*, 235111.

[69] J. Selbin, S. P. McGlynn, *J. Inorg. Nucl. Chem.* **1963**, *25*, 1359.